

Realizing Dark Matter and Higgs Inflation in Light of LHC Diphoton Excess

SHAO-FENG GE ^{*a}, HONG-JIAN HE ^{†b,c}, JING REN ^{‡d}, ZHONG-ZHI XIANYU ^{§e}

^a Max-Planck-Institut für Kernphysik, Heidelberg 69117, Germany

^b Institute of Modern Physics and Center for High Energy Physics, Tsinghua University, Beijing 100084, China

^c Center for High Energy Physics, Peking University, Beijing 100871, China

^d Department of Physics, University of Toronto, Toronto, Ontario, Canada M5S1A7

^e Center of Mathematical Sciences and Applications, and Department of Physics, Harvard University, Cambridge, Massachusetts 02138, USA

Abstract

LHC Run-2 has provided intriguing di-photon signals of a new resonance around 750 GeV, which, if not due to statistical fluctuations, must call for new physics beyond the standard model (SM) at TeV scale. We propose a minimal extension of the SM with a complex singlet scalar S and a doublet of vector-like quarks. The scalar sector respects CP symmetry, with its CP-odd imaginary component χ providing a natural dark matter (DM) candidate. The real component of S serves as the new resonance (750 GeV) and explains the diphoton excess of the LHC Run-2. The new scalar degrees of freedom of S help to stabilize the Higgs vacuum, and can realize the Higgs inflation around GUT scale, consistent with the current cosmological observations. We construct two representative samples A and B of our model for demonstration. We study the mono-jet signals of DM production from invisible decays $\text{Re}(S) \rightarrow \chi\chi$ at the LHC Run-2. We further derive the DM relic density bound, and analyze constraints from the direct and indirect DM detections.

Keywords: LHC, New Resonance, Dark Matter, Higgs Inflation. Phys. Lett. B (2016) in Press [arXiv:1602.01801]

1. Introduction

Both ATLAS and CMS collaborations newly reported intriguing di-photon excess around 750 GeV in pp collisions at the LHC Run-2 [1][2]. With 3.2 fb^{-1} integrated luminosity, ATLAS observed a signal excess at $M_{\gamma\gamma} = 747 \text{ GeV}$ in the di-photon invariant mass distribution with a 3.9σ local significance by assuming a wide resonance width of about 45 GeV. For the narrow resonance assumption, the local significance reduces to 3.6σ . At the same time, CMS collected 2.6 fb^{-1} data set and found a di-photon excess at $M_{\gamma\gamma} = 760 \text{ GeV}$ with 2.6σ local significance under narrow width assumption [2]. When taking this resonance as a narrow-width (pseudo)scalar particle \mathbb{X} produced from gluon fusion, the LHC Run-1 (8 TeV) and Run-2 (13 TeV) data could be combined to yield a di-photon excess, $\sigma[gg \rightarrow \mathbb{X} \rightarrow \gamma\gamma] = (4.6 \pm 1.2) \text{ fb}$, at $M_{\gamma\gamma} \approx 750 \text{ GeV}$ [3]. Despite the 125 GeV Higgs discovery at the LHC Run-1 [4] which seems to complete particle spectrum of the standard model (SM) so far, this new anomaly around $M_{\gamma\gamma} \approx 750 \text{ GeV}$ would point to indisputable evidence of new physics beyond the SM at TeV scale (if not due to statistical fluctuations or systematical errors). Even though the experimental evidence is not yet compelling and more data are expected from the upcoming LHC runs after the spring 2016, it is well-motivated to explore new physics interpretations and implications of such an intriguing anomaly, which will be invaluable guidelines for further experimental tests in this year.

Since only spin-0 or spin-2 particles could decay into di-photons [5], a scalar particle \mathbb{X} with mass $\sim 750 \text{ GeV}$ would be the simplest interpretation of this new resonance. A spin-2 massive Kaluza-Klein graviton will couple to all SM particles with the same strength, and is thus uneasy to explain the absence of di-boson signals of WW/ZZ except the di-photon excess in the current Run-2 data. There are already many recent papers studying various possible explanations with scalar resonance and related new physics [3][6]. In this work, we motivate this new resonance by resolving two existing difficulties of the SM: the vacuum instability and the absence of dark matter (DM) candidate.

*gesf02@gmail.com

†hjhe@tsinghua.edu.cn

‡jren@physics.utoronto.ca

§xianyu@cmsa.fas.harvard.edu

The SM Higgs potential suffers vacuum instability at scales above $\sim 10^{11}$ GeV [7, 8], and new physics is needed to stabilize the vacuum and realize successful cosmic inflation in the early universe. In particular, the most economical approach of inflation is the Higgs inflation [9][10], where the inflaton is identified as the SM Higgs boson, and including proper new physics is required [11, 12]. It was shown before that a minimal extension [12] can save the Higgs inflation by introducing only a real singlet scalar and a vector-like quark at TeV scale. The other serious defect of the SM is its lack of DM candidate to provide the required 28% composition of our universe. For this work, we will present a minimal construction of new physics to resolve three things altogether: (i) consistent realization of Higgs inflation around GUT scale; (ii) natural DM candidate to explain the observed DM relic abundance; (iii) a new scalar state with mass ~ 750 GeV to induce the enhanced di-photon excess at the LHC Run-2 [1][2]. For this purpose, our minimal extension includes a complex singlet scalar \mathcal{S} and a doublet of vector-like quarks with electric charges $(\frac{5}{3}, \frac{2}{3})$. The scalar sector respects CP symmetry, with the SM-like light Higgs boson h (125 GeV) acting as the inflaton in the early universe. The CP-odd imaginary component $\text{Im}(\mathcal{S})$ provides a stable DM candidate, while the real component $\text{Re}(\mathcal{S})$ serves as the new resonance (750 GeV), which is produced by gluon fusion via vector-quark triangle loops, with di-photon decays to give the observed LHC excess. The new scalar degrees of freedom of \mathcal{S} help to stabilize the Higgs vacuum, and thus realize successful Higgs inflation around GUT scale, consistent with the current cosmology observation.

This paper is organized as follows. In section 2, we construct a minimal extension with a complex singlet scalar \mathcal{S} and a doublet of vector-like quarks $(\mathcal{T}', \mathcal{T})^T$ at TeV scale. Then, in section 3 we study the decays and production of the CP-even component of \mathcal{S} , and realize the observed LHC di-photon signals at $M_{\gamma\gamma} \simeq 750$ GeV. For explicit demonstration, we will construct two representative samples A and B. Section 4 is devoted to analyzing vacuum stability of the new Higgs potential, and realizing a consistent Higgs inflation. Next, we systematically analyze the CP-odd component of \mathcal{S} as the DM candidate in section 5, where we will realize the observed DM relic abundance in Sec. 5.1, and study the DM production at the LHC Run-2 (Sec. 5.2), the DM direct detection (Sec. 5.3), and the DM indirect detection (Sec. 5.4). Finally, we conclude in section 6. Appendix A provides the needed formulas for the $\text{Re}(\mathcal{S})$ partial decay widths, while Appendix B presents the additional one-loop β functions induced by the new scalar couplings and new Yukawa coupling.

2. Model Setup with Singlet Scalar and Vector-like Quarks

In this section, we construct a minimal model by implementing a complex scalar singlet \mathcal{S} and a doublet of vector-like quarks $(\mathcal{T}', \mathcal{T})^T$ at TeV scale. As mentioned in Sec. 1, this can nicely tie three new physics ingredients altogether: the consistent realization of Higgs inflation with the SM-like Higgs boson h (125 GeV) acting as inflaton, a stable DM candidate $\text{Im}(\mathcal{S})$, and a new scalar $\text{Re}(\mathcal{S})$ of mass 750 GeV. Hence, the newly observed di-photon excess from a 750 GeV resonance decays at the LHC Run-2 can link our predictions to the on-going DM detections and the probe of Higgs inflation in the early universe.

Our Higgs sector consists of the SM Higgs doublet H and a complex scalar singlet \mathcal{S} , defined as follows,

$$H = \begin{pmatrix} \pi^+ \\ \frac{v+h_0+i\pi_0}{\sqrt{2}} \end{pmatrix}, \quad \mathcal{S} = \frac{u + S_0 + i\chi}{\sqrt{2}} \equiv \mathcal{S}_+ + i\mathcal{S}_-, \quad (2.1)$$

where v and u denote the corresponding vacuum expectation values (VEV) of H and \mathcal{S} . Both the real and imaginary components, \mathcal{S}_+ and \mathcal{S}_- , can help to stabilize the Higgs potential. Under the CP transformation, we have $\mathcal{S} \rightarrow \mathcal{S}^*$, which means $(\mathcal{S}_+, \mathcal{S}_-) \rightarrow (\mathcal{S}_+, -\mathcal{S}_-)$. Namely, \mathcal{S}_+ (S_0) is CP-even and \mathcal{S}_- (χ) is CP-odd. Our construction imposes CP symmetry on the Higgs potential as well as the Yukawa interactions of singlet \mathcal{S} . As shown in Table 1, we will further impose a separate \mathbb{Z}_2 symmetry, under which the Higgs doublet H is even, and the singlet $(\mathcal{S}_+, \mathcal{S}_-) \rightarrow (-\mathcal{S}_+, \mathcal{S}_-)$, i.e., $\mathcal{S} \rightarrow -\mathcal{S}^*$. Thus, the building blocks of constructing a gauge-invariant and $\text{CP} \otimes \mathbb{Z}_2$ symmetric Higgs potential contain $H^\dagger H$, $(\mathcal{S} + \mathcal{S}^*)^2$, and $(\mathcal{S} - \mathcal{S}^*)^2$, where the second and third combinations are proportional to \mathcal{S}_+^2 and \mathcal{S}_-^2 , respectively. Hence, we can write down the following gauge-invariant and $\text{CP} \otimes \mathbb{Z}_2$ symmetric Higgs potential for (H, \mathcal{S}) ,

$$V(H, \mathcal{S}) = -\mu_1^2 H^\dagger H - \mu_2^2 \mathcal{S}_+^2 + \lambda_1 (H^\dagger H)^2 + \lambda_2 \mathcal{S}_+^4 + \lambda_3 \mathcal{S}_+^2 H^\dagger H \\ + \mu_3^2 \mathcal{S}_-^2 + \lambda_4 \mathcal{S}_-^4 + \lambda_5 \mathcal{S}_+^2 \mathcal{S}_-^2 + \lambda_6 \mathcal{S}_-^2 H^\dagger H, \quad (2.2)$$

where all masses and couplings are real. We see that in the basis $(\mathcal{S}_+, \mathcal{S}_-)$, the first line of our Higgs potential (2.2) corresponds to the original Higgs potential in Ref. [12] with a real singlet scalar. Since the CP-odd pseudoscalar \mathcal{S}_- has a positive mass-term $+\mu_3^2$ in the potential (2.2), so it ensures a vanishing VEV of \mathcal{S}_- and keep the CP symmetry intact in the scalar sector. The CP-odd pseudoscalar \mathcal{S}_- will serve as a stable DM candidate, as to be analyzed in Sec. 5. Note that scalar VEVs (v, u) in (2.1) do not affect CP invariance, except spontaneously breaking \mathbb{Z}_2 . Since the

Table 1: Quantum number assignments for the Higgs doublet H , the singlet scalar \mathcal{S} , the vector-like quark doublet $\mathbb{T} = (\mathcal{T}', \mathcal{T})^T$, and the SM quarks, under the SM gauge group $SU(3)_C \otimes SU(2)_L \otimes U(1)_Y$ and the discrete \mathbb{Z}_2 . All other fields have the same assignments as in the SM. Here $j (= 1, 2)$ stands for the indices of first and second family quarks, with $Q_{jL} = (u_j, d_j)_L^T$ and $Q_{3L} = (t, b)_L^T$.

Groups	Q_{jL}	u_{jR}	d_{jR}	Q_{3L}	t_R	b_R	H	\mathbb{T}_L	\mathbb{T}_R	$(\mathcal{S}_+, \mathcal{S}_-)$
$SU(3)_C$	3	3	3	3	3	3	1	3	3	1
$SU(2)_L$	2	1	1	2	1	1	2	2	2	1
$U(1)_Y$	$\frac{1}{6}$	$\frac{2}{3}$	$-\frac{1}{3}$	$\frac{1}{6}$	$\frac{2}{3}$	$-\frac{1}{3}$	$\frac{1}{2}$	$\frac{7}{6}$	$\frac{7}{6}$	0
\mathbb{Z}_2	+	+	+	-	-	-	+	+	-	(-, +)

mass term of vector-like heavy quarks [cf. Eq. (2.3)] will softly break \mathbb{Z}_2 and contribute to the Higgs potential at loop level, this model is free from the domain wall problem.

To explain the observed 750 GeV excess of diphoton signals from $gg \rightarrow S_0 \rightarrow \gamma\gamma$, the simplest natural resolution is to couple it with certain charged quarks. But, a scalar singlet \mathcal{S} cannot have gauge-invariant and renormalizable Yukawa interactions with the SM fermions. Furthermore, the LHC Run-2 has not found S_0 decays into the SM fermions so far. Hence, it is natural to couple the singlet \mathcal{S} to certain new heavy quarks. In our construction, we introduce a pair of vector-like quarks $\mathbb{T} = (\mathcal{T}', \mathcal{T})^T$, which compose a weak doublet under the SM gauge group $SU(2)_L$. (The doublet vector-like quarks were invoked in model-buildings before [13] with the SM hypercharge $Y = 1/6$. For the present model, we extend it to have hypercharge $Y = 7/6$. This assignment was also considered in [14].) The vector-like quarks $(\mathcal{T}', \mathcal{T})$ will induce production and decays of the new scalar S_0 via triangle loops. We arrange the quantum number assignments of our model in Table 1, where we have imposed a \mathbb{Z}_2 symmetry to restrict the additional Yukawa interactions involving the vector-like quark doublet \mathbb{T} and/or singlet scalar \mathcal{S} . We conjecture that the singlet \mathcal{S} interactions always conserve CP, and all interaction forces respect \mathbb{Z}_2 . So the \mathbb{Z}_2 symmetry could be softly broken only via the bare mass term of the vector-like quark doublet \mathbb{T} .

The observed sizable di-photon rate at $M_{\gamma\gamma} \approx 750$ GeV and the absence of dijet excess in the same mass region so far suggests that the new resonance S_0 should have enhanced decay rate into di-photons. This indicates that the heavy quarks may have larger electric charges and thus enhanced couplings with di-photons. For this, we introduce a weak doublet of vector-like quarks, $\mathbb{T} = (\mathcal{T}', \mathcal{T})^T$, with hypercharge $Y = \frac{7}{6}$ and thus the electric charges $(\frac{5}{3}, \frac{2}{3})$, where the heavy quark \mathcal{T} shares the same electric charge with the SM up-type quarks.

According to the model construction in Table 1, we write down the relevant Yukawa interactions including the Yukawa interaction between the vector-like quark doublet \mathbb{T} and singlet scalar \mathcal{S} , as well as the Yukawa interactions between \mathbb{T} and light SM up-type quarks,

$$\mathcal{L}_{\mathbb{T}u} = -y_{ij}\bar{Q}_{iL}\bar{H}u_{jR} - \tilde{y}_j\bar{\mathbb{T}}_L H u_{jR} - \frac{1}{2}\tilde{y}_S\mathcal{S}_+\bar{\mathbb{T}}\mathbb{T} - \frac{1}{2}M_0\bar{\mathbb{T}}\mathbb{T} + \text{h.c.}, \quad (2.3)$$

where $\bar{H} = i\tau_2 H^*$, and $i, j = 1, 2$ stand for flavor indices of the first and second family fermions. We see that \mathbb{T} does not mix with third family top quark due to \mathbb{Z}_2 symmetry. The Yukawa coupling \tilde{y}_S in Eq. (2.3) is real, since the singlet \mathcal{S} interactions conserve CP. Besides, all interactions respect \mathbb{Z}_2 symmetry, and the only possible soft breaking term of \mathbb{Z}_2 is the bare mass term (M_0) of vector-like quark doublet \mathbb{T} . Eq. (2.3) gives the following mixing mass matrix for u_j ($j = 1, 2$) and \mathcal{T} ,¹

$$M_{u_j\mathcal{T}} = \frac{1}{\sqrt{2}} \begin{pmatrix} y_{11}^v & y_{12}^v & 0 \\ y_{21}^v & y_{22}^v & 0 \\ \tilde{y}_1^v & \tilde{y}_2^v & \tilde{y}_S u + \sqrt{2}M_0 \end{pmatrix}, \quad (2.4)$$

where the (3, 3)-component contains both the VEV contribution term $\tilde{y}_S u/\sqrt{2}$ [from the third term of Eq. (2.3)] and the bare mass term M_0 [from the fourth term of Eq. (2.3)]. For our purpose, we consider the parameter space of $\tilde{y}_j^v \ll \tilde{y}_S u + \sqrt{2}M_0$. Taking the small non-diagonal couplings $\tilde{y}_{1,2}$ being comparable, we estimate the small mixing of

¹We also note that the small quark mixings between the light families and the third family can arise from dimension-5 effective operators involving singlet scalar, $(y_{ii}/\Lambda)S_+\bar{Q}_{iL}\bar{H}t_R$ and $(y_{ib}/\Lambda)S_+\bar{Q}_{iL}\bar{H}b_R$, where $i = 1, 2$ and Λ is the cutoff. Such effective operators will induce the desired small CKM mixings. They may result from integrating out a heavy Higgs doublet H' which is \mathbb{Z}_2 odd and can realize dimension-4 Yukawa terms between the light families and the third family, $y'_{ii}\bar{Q}_{iL}\bar{H}'t_R$ and $y'_{ib}\bar{Q}_{iL}\bar{H}'b_R$. Adding this heavy Higgs doublet H' will increase the scalar degrees of freedom and make vacuum stability much easier, but does not change the main physics picture. For the current purpose of accommodating the diphoton excess, we focus on the minimal setup for simplicity.

\mathcal{T} and u_j , $\theta_{Lj} \approx y_{jj}\tilde{y}_j v^2 / (\tilde{y}_S u + \sqrt{2}M_0)^2$ for the left-handed quarks, and $\theta_{Rj} \approx \tilde{y}_j v / (\tilde{y}_S u + \sqrt{2}M_0)$ for the right-handed quarks. Thus, we have nearly degenerate heavy quarks,

$$M_{\mathcal{T}'} \approx M_{\mathcal{T}} \approx \frac{1}{\sqrt{2}}\tilde{y}_S u + M_0. \quad (2.5)$$

The small mixing couplings \tilde{y}_j will induce \mathcal{T} and \mathcal{T}' decays. The heavy quark \mathcal{T} has two main decay channels, $\mathcal{T} \rightarrow u_j h$ and $\mathcal{T} \rightarrow d_j W^+$, while \mathcal{T}' dominantly decays via $\mathcal{T}' \rightarrow u_j W^+$. We find that for channels $\mathcal{T} \rightarrow d_j W^+, u_j Z$ and $\mathcal{T}' \rightarrow u_j W^+$, the decay amplitudes are dominated by the final state with longitudinal polarization W_L^+ . Since $M_{\mathcal{T}} \gg M_W$, we can apply equivalence theorem [15] to compute the corresponding Goldstone amplitudes with W_L^+ replaced by π^+ . Thus, we estimate the leading decay width for each channel as follows,

$$\Gamma[\mathcal{T} \rightarrow u_j h] \approx \frac{\tilde{y}_j^2}{16\pi} M_{\mathcal{T}}, \quad \Gamma[\mathcal{T} \rightarrow d_j W^+, u_j Z] \approx \frac{y_{jj}^2 \theta_{Rj}^2}{32\pi} M_{\mathcal{T}}, \quad \Gamma[\mathcal{T}' \rightarrow u_j W^+] \approx \frac{\tilde{y}_j^2}{32\pi} M_{\mathcal{T}'}. \quad (2.6)$$

It is clear that $\mathcal{T} \rightarrow u_j h$ is the dominant decay mode for \mathcal{T} . For later analysis, we will consider the parameter range, $10^{-5} \lesssim \tilde{y}_j \lesssim 10^{-3}$. This is sufficient to evade the flavor constraints involving the first two family quarks, and the tiny mixing coupling \tilde{y}_j is negligible in our later analysis of renormalization group running and collider studies. Furthermore, this ensures that the lifetimes of \mathcal{T} and \mathcal{T}' are much smaller than 10^{-13} s. So they are short-lived and will have prompt decays inside the detector [16]. The searches of heavy vector-like quarks via prompt decays put nontrivial constraints on the new quark masses. The limits on their decays into a light quark are weaker than that into top or bottom. For $\mathcal{T}' \rightarrow u_j W^+$, the limit is $M_{\mathcal{T}'} \gtrsim 690$ GeV, while the decay channel $\mathcal{T} \rightarrow u_j h$ is much less constrained [17].

3. New Particle Decays and Production

In the physical vacuum, the Higgs doublet H and singlet S acquire nonzero VEVs, as shown in (2.1). This spontaneously breaks $SU(2)_L \otimes U(1)_Y \otimes \mathbb{Z}_2$ down to $U(1)_{\text{em}}$, while the CP symmetry is retained. The CP-even states (h_0, S_0) can mix with each other via $h = c_\alpha h_0 + s_\alpha S_0$ and $S = c_\alpha S_0 - s_\alpha h_0$, where $(c_\alpha, s_\alpha) \equiv (\cos \alpha, \sin \alpha)$. The mixing angle α is determined by diagonalizing the mass matrix,

$$M_N^2 = \begin{pmatrix} 2\lambda_1 v^2 & \lambda_3 v u \\ \lambda_3 v u & 2\lambda_2 u^2 \end{pmatrix}, \quad \Rightarrow \quad (M_N^2)_{\text{diag}} = \begin{pmatrix} M_h^2 & 0 \\ 0 & M_S^2 \end{pmatrix}, \quad (3.1)$$

with

$$\tan 2\alpha = \frac{\lambda_3 v u}{\lambda_1 v^2 - \lambda_2 u^2}. \quad (3.2)$$

Alternatively, we may resolve the 3 involved scalar couplings $(\lambda_1, \lambda_2, \lambda_3)$ in terms of the measured mass-eigenvalues $(M_h, M_S) \simeq (125, 750)$ GeV, the known light Higgs VEV $v \simeq 246$ GeV, and the Higgs mixing angle α (which is taken as an input parameter, but will be constrained by the LHC data). Thus, we have,

$$\lambda_1 = \frac{M_h^2 c_\alpha^2 + M_S^2 s_\alpha^2}{2v^2}, \quad \lambda_2 = \frac{M_S^2 c_\alpha^2 + M_h^2 s_\alpha^2}{2u^2}, \quad \lambda_3 = \frac{s_\alpha c_\alpha (M_h^2 - M_S^2)}{uv}. \quad (3.3)$$

Although the singlet scalar S does not couple to the SM fermions and gauge bosons, the mixing between the two CP-even components S_0 and h_0 will induce these couplings suppressed by $\sin \alpha$. Table 2 summarizes the coupling ratios ξ_{hXY} and ξ_{SXY} relative to the SM counterparts, for the mass-eigenstates h and S .

Inspecting the cubic scalar coupling of $S h h$ vertex and using Eq. (3.3), we derive its compact form as follows,

$$G_{Shh} = \frac{s_\alpha c_\alpha (u c_\alpha - v s_\alpha)}{uv} (M_S^2 + 2M_h^2). \quad (3.4)$$

Table 2: Coupling ratios ξ_{hXY} and ξ_{SXY} of the Higgs bosons h and S , relative to the SM counterparts, where $V = W, Z$, and the SM Yukawa coupling is $y_f = m_f/v$.

XY	$f\bar{f}$	VV	$T\bar{T}$
ξ_{hXY}	c_α	c_α	$s_\alpha (\tilde{y}_S/y_t)$
ξ_{SXY}	$-s_\alpha$	$-s_\alpha$	$c_\alpha (\tilde{y}_S/y_t)$

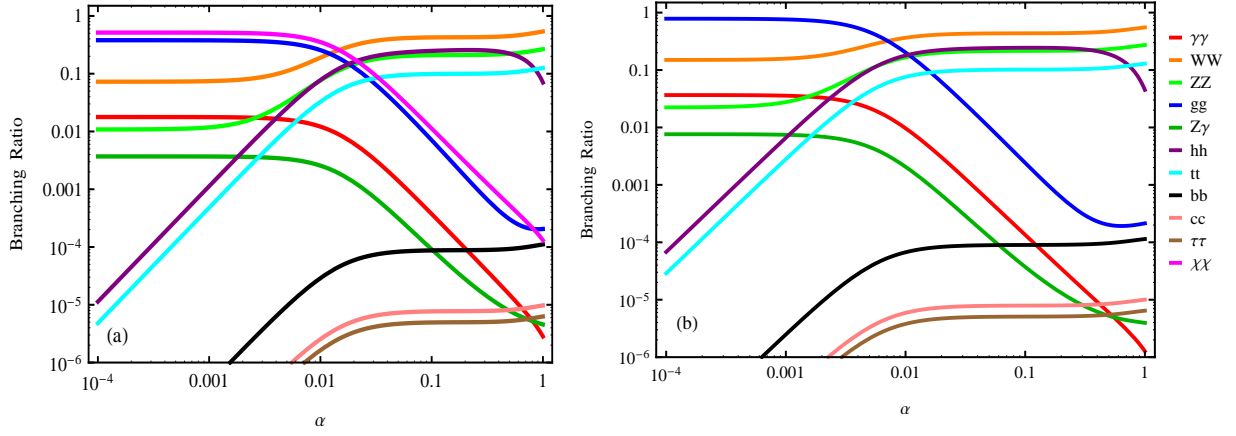


Figure 1: Decay branching fractions of CP-even state S (750 GeV) as a function of Higgs mixing angle α . We have input masses $M_{\mathcal{T}} \simeq M_{\mathcal{T}'} = 720$ GeV for both plots, as well as the VEV $u = 0.57$ [1.2] TeV and Yukawa coupling $\tilde{y}_S = 1.5$ [0.88] for plot-(a)-(b), which are motivated by Sample-A [-B] of Eq. (3.5). In plot-(a) the invisible decay channel $S \rightarrow \chi\chi$ is open under input $M_\chi = 240$ GeV, while this channel is forbidden in plot-(b) due to $M_\chi > M_S/2$.

Clearly, this coupling is suppressed by s_α for small mixing angle α . Hence, the decay width of $S \rightarrow hh$ is proportional to s_α^2 and will become negligible as $\alpha \rightarrow 0$.

With Table 2 and Eq. (3.4), we implement S couplings into the decay width formula (A.1), and compute the branching fractions of the CP-even state S as a function of Higgs mixing angle α . Then, we present the S decay branching fractions in Fig. 1. For a sizable mixing angle α , we expect S decays into the SM fermions and gauge bosons to be significant. Fig. 1 shows that for $\alpha \gtrsim 0.01$, the decay channels $S \rightarrow WW, ZZ, hh$ and $S \rightarrow t\bar{t}$ dominate, while $S \rightarrow \gamma\gamma$ and $S \rightarrow gg$ channels become much suppressed. Hence, we see that in order to obtain a sizable branching fraction $\text{Br}[S \rightarrow \gamma\gamma]$ for enhanced diphoton rate at the LHC, the Higgs mixing angle α should be fairly small, within the range of $\alpha < 0.01$.

In the limit $\alpha \sim 0$ with the fixed VEV u , we have, $\lambda_3 \sim 0$, $\lambda_1 \sim M_h^2/(2v^2)$, and $\lambda_2 \sim M_S^2/(2u^2)$, according to Eq. (3.3). This implies that the two CP-even states h and S nearly decouple from each other. To summarize, imposing two extremal conditions on the Higgs potential V , taking a small Higgs mixing angle α , inputting the VEV v ($\simeq 246$ GeV), and fixing Higgs masses $(M_h, M_S) \simeq (125, 750)$ GeV, we have 6 conditions in total. Thus, we can determine 6 parameters (μ_1, μ_2, u) and $(\lambda_1, \lambda_2, \lambda_3)$ in the Higgs potential (2.2). We are left with 4 free parameters $(\mu_3, \lambda_4, \lambda_5, \lambda_6)$ associated with masses and couplings of the CP-odd state χ . We will use them to realize the viable Higgs inflation and DM in Sec. 4 and Sec. 5, respectively.

For demonstration, we construct two numerical samples for our phenomenological study. In both samples, we set inputs, $M_S = 750$ GeV, $\alpha = 10^{-3}$, and $\theta_{L,R} \simeq 0$. The rest of parameters are defined as follows,

$$\text{Sample-A: } u = 0.57 \text{ TeV, } M_{\mathcal{T}} \simeq M_{\mathcal{T}'} = 720 \text{ GeV, } \tilde{y}_S = 1.5, \lambda_4 = 0.4, \lambda_5 = 0.1, \lambda_6 = 0.08; \quad (3.5a)$$

$$\text{Sample-B: } u = 1.2 \text{ TeV, } M_{\mathcal{T}} \simeq M_{\mathcal{T}'} = 720 \text{ GeV, } \tilde{y}_S = 0.88, \lambda_4 = 0.1, \lambda_5 = 0.3, \lambda_6 = 0.2; \quad (3.5b)$$

where the couplings $(\tilde{y}_S, \lambda_4, \lambda_5, \lambda_6)$ are defined at a renormalization scale $\mu = M_S$. The DM mass M_χ is irrelevant to the analysis of vacuum stability and perturbativity. But for the following LHC analysis and for the DM detection analysis in Sec. 5, we will define $M_\chi < M_S/2$ in Sample-A and $M_\chi > M_S/2$ in Sample-B. For the masses of heavy vector-like quarks, we choose a benchmark value above the current lower bound on $M_{\mathcal{T}'}$ (shown in Sec. 2). Our goal is to accommodate the observed excess of diphoton rate, with reasonable S Yukawa coupling which is consistent with the requirements of stability and perturbativity. Since $M_{\mathcal{T}}$ and $M_{\mathcal{T}'}$ include contribution from the bare mass term (M_0), the diphoton rate is not connected to the simple ratio of mass $M_{\mathcal{T}}$ and VEV u . Thus, we can properly choose u according to the desired value of λ_2 . We construct Sample-A and -B for different purposes here. Sample-A has $M_\chi < 375$ GeV, which can produce both the diphoton excess and the invisible decay $S \rightarrow \chi\chi$, and have the vacuum instability bound much higher than TeV scale at the same time. If assume no invisible decay, we derive a sizable diphoton cross section at the LHC Run-2 as follows,

$$\sigma(pp \rightarrow S \rightarrow \gamma\gamma) = 7.3 \text{ fb,} \quad (\text{Sample-A}), \quad (3.6)$$

where the parton distribution function MSTW08 [18] is used. This is higher than the central value of fitted diphoton signals [3] of Run-2 data [1][2]. After the invisible decay channel $S \rightarrow \chi\chi$ is open, we find that for $M_\chi = 100 - 350$ GeV, the diphoton cross section varies within the range,

$$\sigma(pp \rightarrow S \rightarrow \gamma\gamma) = 3.1 - 4.9 \text{ fb,} \quad (\text{Sample-A}). \quad (3.7)$$

This is consistent with the recent fit of combined LHC Run-2 and Run-1 diphoton rate [3], $\sigma[gg \rightarrow \mathbb{X} \rightarrow \gamma\gamma] = 4.6 \pm 1.2 \text{ fb}$, well within the 2σ range. We will further analyze the invisible decay channel in Sec. 5.2. For Sample-B, we consider $M_\chi > 375 \text{ GeV}$, and optimize the parameters to accommodate both the diphoton excess and the Higgs inflation, which maintains the vacuum stability and perturbativity up to the inflation scale. Thus, we compute

$$\sigma(pp \rightarrow S \rightarrow \gamma\gamma) = 2.5 \text{ fb}, \quad (\text{Sample-B}), \quad (3.8)$$

which is consistent with the recent fit of LHC diphoton rate [3] and well within the 2σ range. The non-observation of the 750 GeV resonance in the di-jet channel ($S \rightarrow gg$) so far could give important constraint. In our model, for $\alpha \lesssim 10^{-3}$, we find,

$$\sigma(pp \rightarrow S \rightarrow gg) \simeq 21\sigma(pp \rightarrow S \rightarrow \gamma\gamma). \quad (3.9)$$

This is far below the CMS constraint on the di-jet cross section ($< 1.8 \text{ pb}$) by using the LHC Run-1 data [19]. Another loop-induced channel is the rare decay $S \rightarrow Z\gamma$. In our model, its cross section is much smaller than that of the diphoton final state, and is well below the current constraint [20]. For $S \rightarrow hh, t\bar{t}, b\bar{b}$ decay modes, the signal rates are negligibly small in the $\alpha \sim 10^{-3}$ region. In this α range, $S \rightarrow WW, ZZ$ are mainly induced by the $\mathcal{T} (\mathcal{T}')$ triangle loops, and we find the following relations,

$$\sigma(pp \rightarrow S \rightarrow WW) \simeq 4.3\sigma(pp \rightarrow S \rightarrow \gamma\gamma), \quad \sigma(pp \rightarrow S \rightarrow ZZ) \simeq 0.65\sigma(pp \rightarrow S \rightarrow \gamma\gamma). \quad (3.10)$$

Note that for all the loop induced decay modes, $S \rightarrow \gamma\gamma, gg, WW, ZZ$, the relative sizes are fixed by the gauge quantum numbers of the heavy vector-like quarks ($\mathcal{T}', \mathcal{T}$). The LHC Run-1 data imposed upper limits on WW and ZZ final states [21]. These limits may be converted into bounds on the cross sections at the LHC Run-2 (13 TeV), implying that the upper bounds on WW and ZZ cross sections around the 750 GeV region are roughly 220 fb and 56 fb , respectively [22]. They are far above our prediction (3.10) inferred from the diphoton signals.

4. Vacuum Stability and Higgs Inflation

A principal motivation of our model is to ensure the stability of Higgs potential in the very early universe when the scale of energy density is much higher than the weak scale. We recall that, in general, a scalar coupling tends to stabilize the potential while a Yukawa coupling tends to destabilize it. In our model, this means in particular that the new Yukawa coupling \tilde{y}_S should not be too large. We find that Sample-B does meet this criterion to maintain vacuum stability up to inflation scale. In Sec. 4.1, we first study the vacuum stability for both samples A and B. Then, in Sec. 4.2, we take the advantage of Sample-B to realize successful Higgs inflation.

4.1. Renormalization Group Running and Vacuum Stability

The vacuum stability may be studied by directly computing the effective Higgs potential with loop corrections, or by resumming up loop corrections into running couplings of the tree-level Higgs potential via renormalization group (RG). We will use the RG approach for the current analysis. Thus, we can apply the tree-level stability condition to the running scalar couplings and derive stability bound on the allowed running energy scale. For our model, the vacuum stability is mainly dictated by the competition of running contributions between scalar loops (involving scalar self-couplings) and fermion loops (involving the top and \mathbb{T} Yukawa couplings), since the contributions from gauge couplings (g_s, g, g') are minor. Inspecting the Higgs potential (2.2), we have the tree-level stability conditions,

$$\begin{aligned} \lambda_{1,2,4} &\geq 0, & \lambda_3 &\geq -2\sqrt{\lambda_1\lambda_2}, & \lambda_6 &\geq -2\sqrt{\lambda_1\lambda_4}, & \lambda_5 &\geq -2\sqrt{\lambda_2\lambda_4}, \\ 2\lambda_1\lambda_5 - \lambda_3\lambda_6 &\geq -\sqrt{(4\lambda_1\lambda_2 - \lambda_3^2)(4\lambda_1\lambda_4 - \lambda_6^2)}. \end{aligned} \quad (4.1)$$

To further realize Higgs inflation, we consider the joint effective theory which combines our model (Table 1) with the general relativity, and includes the unique dimension-4 non-minimal coupling term $\xi RH^\dagger H$, where R is the Ricci scalar curvature. As before [12], we will use the SM two-loop β functions together with the one-loop β functions of the non-minimal coupling ξ and other couplings involving new scalars and new fermions, including the s factor which arises from the non-minimal coupling term [12, 23, 24]. The two-loop β functions of SM with s insertions and the one-loop β function for ξ were given in [12, 24]. We present the contributions to the β functions by the new couplings in Appendix B. The one-loop matching at top mass is done as described in [25].

With these, we analyze the RG runnings for Sample-A and Sample-B, and derive the vacuum stability bounds for the Higgs potential. In Fig. 2(a)-(b) and Fig. 2(c)-(d), we present the running scalar couplings as functions of the renormalization scale μ . For Sample-A, we find that the stability bound is reached around $\mu \simeq 5.4 \times 10^3 \text{ TeV}$, due

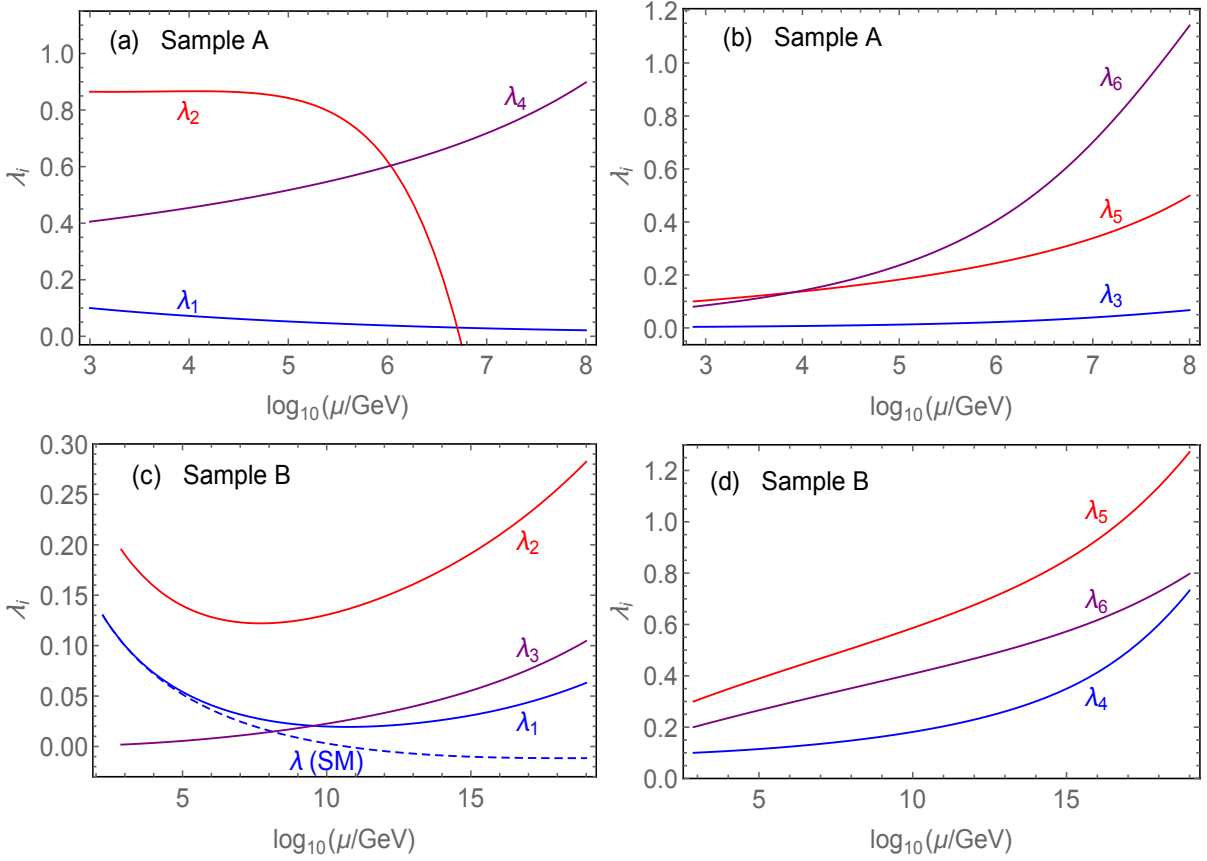


Figure 2: Running scalar couplings λ_i of the present model as functions of the RG scale μ . Plots (a)-(b) show the running behaviors for Sample-A, while plots (c)-(d) depict that for Sample-B. The dashed curve in plot (c) represents the SM Higgs self-coupling λ up to two-loop RG.

to the decrease of λ_2 , as shown in Fig. 2(a). For Sample-B, we find that all scalar couplings remain positive and perturbative up to Planck scale. This ensures the Higgs potential to be a valid description of the inflation potential, so the inflation trajectory is stable against small perturbations in the directions of (S, χ) .

In both Samples A and B, we fix the singlet mass as $M_S = 750$ GeV. It would also be instructive to inspect how the vacuum stability in our samples is affected by varying the singlet mass around $M_S = 750$ GeV. We can clearly check this effect through the one-loop β functions (B.1) and (B.2). The main concern of the Higgs vacuum stability in the SM model is the running of λ_1 , which may drive λ_1 into negative value at high energies. This problem is relieved in our model due to the positive contribution of β_{λ_1} from λ_3 and λ_6 . The main contribution actually comes from λ_6 , since the smallness of mixing angle α requires λ_3 be tiny, as can be seen from Eq. (3.3). On the other hand, since λ_3 is tiny, from (3.1) we see that varying M_S mainly affects the value of λ_2 . But, Eq. (B.2) shows that the one-loop β_{λ_6} does not depend on λ_2 explicitly. So it is clear that the vacuum stability is very insensitive to the variation of M_S . We also check this numerically by varying M_S in Sample B, and find that the vacuum stability is well preserved over the mass range $700 \text{ GeV} \leq M_S \leq 800 \text{ GeV}$ (with other parameters fixed).

4.2. Realizing Higgs Inflation

In Higgs inflation, it is the Higgs field that successfully drives the cosmic inflation, and the same Higgs field will spontaneously break the electroweak gauge symmetry at low energies. The typical energy density scale during Higgs inflation is around 10^{16} GeV. Hence, for our model to hold consistently up to the inflation scale, the RG running will play an essential role. We have done the RG running analysis in Sec. 4.1. Fig. 2(c)-(d) shows that Sample-B is a possible candidate for realizing successful Higgs inflation. In this subsection, we will apply this to directly derive the Higgs inflation potential and inflationary observables.

In Higgs inflation, the unique non-minimal coupling term $\xi RH^\dagger H$ plays the key role to flatten the Higgs potential at high energies. It is conventional to work in the Einstein frame, and we find that the Higgs inflation occurs along the valley of the Higgs potential where the fields $(S, \chi) = (0, 0)$. In Einstein frame, we express the Higgs field h in terms of canonically normalized field φ , through $d\varphi/dh = (\Omega^2 + 6\xi^2 h^2/M_{\text{pl}}^2)^{1/2}/\Omega^2$. Here $\Omega^2 = 1 + \xi h^2/M_{\text{pl}}^2$ is the Weyl factor that brings the action from its defining (Jordan) frame to the Einstein frame, and $M_{\text{pl}} \simeq 2.4 \times 10^{18}$ GeV is

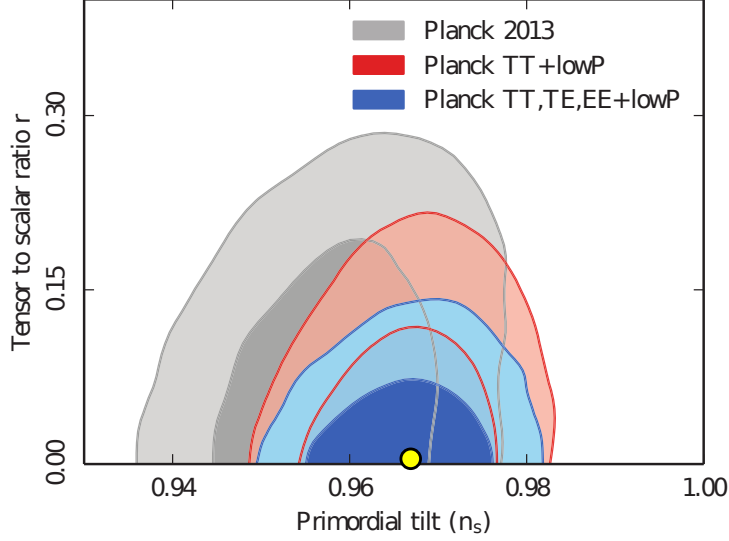


Figure 3: Predicted scalar tilt n_s and tensor-to-scalar ratio r by the present model (shown as the yellow dot), in comparison with various Planck limits in 2015 and 2013 [28]. In each type of contours, the shaded darker and lighter regions represent the 68% and 95% limits, respectively.

the reduced Planck mass. Thus, we can rewrite the Higgs potential in terms of the normalized field φ , and expand it in the large field region ($h \gg M_{\text{Pl}}/\xi$),

$$V(\varphi) \simeq \frac{\lambda_1 M_{\text{Pl}}^2}{4\xi^2} \left(1 - e^{-\sqrt{2/3}\varphi/M_{\text{Pl}}}\right)^2, \quad (4.2)$$

From this potential, we can directly compute the first two slow-roll parameters, ϵ and η , as well as the number of e -foldings N_e between the beginning and end of the observable inflation,

$$\epsilon = \frac{M_{\text{Pl}}^2}{2} \frac{V_\varphi'^2}{V^2}, \quad \eta = M_{\text{Pl}}^2 \frac{V_\varphi''}{V}, \quad N_e = \frac{1}{M_{\text{Pl}}} \int_{\varphi_{\text{end}}}^{\varphi_0} \frac{d\varphi}{\sqrt{2\epsilon}}. \quad (4.3)$$

Here we use φ_0 and φ_{end} to denote the values of the inflaton field φ at the beginning and end of the observable inflation. The condition for ending the inflation is given by $\epsilon < 1$ in our model, and the beginning of observable inflation can then be determined by the needed number of e -foldings, which is $N_e \simeq 59$ for typical Higgs inflation [26]. Then, we derive the inflation observables, including the scalar amplitude $(V/\epsilon)^{1/4}$, the scalar tilt $n_s = 1 - 6\eta + 2\epsilon$, and the tensor-to-scalar ratio $r = 16\epsilon$, at $\varphi = \varphi_0$. The inflation potential $V(\varphi)$ contains one free parameter, the non-minimal coupling ξ , and it can be fixed by the Planck normalization for the scalar amplitude $(V/\epsilon)^{1/4}$ [27]. In our Sample-B, this corresponds to $\xi \simeq 8000$. Then, we derive the predicted scalar tilt n_s and tensor-to-scalar ratio r ,

$$n_s \simeq 0.967, \quad r \simeq 0.004, \quad (\text{Sample-B}). \quad (4.4)$$

We compare these predictions with the announced Planck limits [28] and find good agreement. This comparison is presented in Fig. 3.

5. Realizing Dark Matter: Relic Abundance and Searches

In this section, we analyze the realization of the CP-odd singlet χ as the DM candidate. We further study its searches at the LHC and its (in)direct detections. Sec. 5.1 analyzes the relic abundance for the DM χ , and derives nontrivial constraints on the DM mass for both Sample-A and Sample-B. Then, Sec. 5.2 studies the DM collider signals via invisible decays of the 750 GeV new resonance ($S \rightarrow \chi\chi$) for Sample-A at the LHC Run-2. Finally, we analyze the DM direct and indirect detections in Sec. 5.3–5.4.

5.1. Dark Matter Relic Abundance

The singlet pseudoscalar χ serves as the DM candidate in our model. It only couples to scalar particles via the Higgs potential (2.2). For the DM annihilation processes, if the intermediate particle is S , the final state particles can be $gg, hh, hS, SS, \mathcal{T}\mathcal{T}$ and $\mathcal{T}'\mathcal{T}'$, depending on whether the DM mass is large enough to open the relevant channels. On the other hand, if the intermediate particle is the light Higgs boson h , then $\chi\chi$ will annihilate into SM

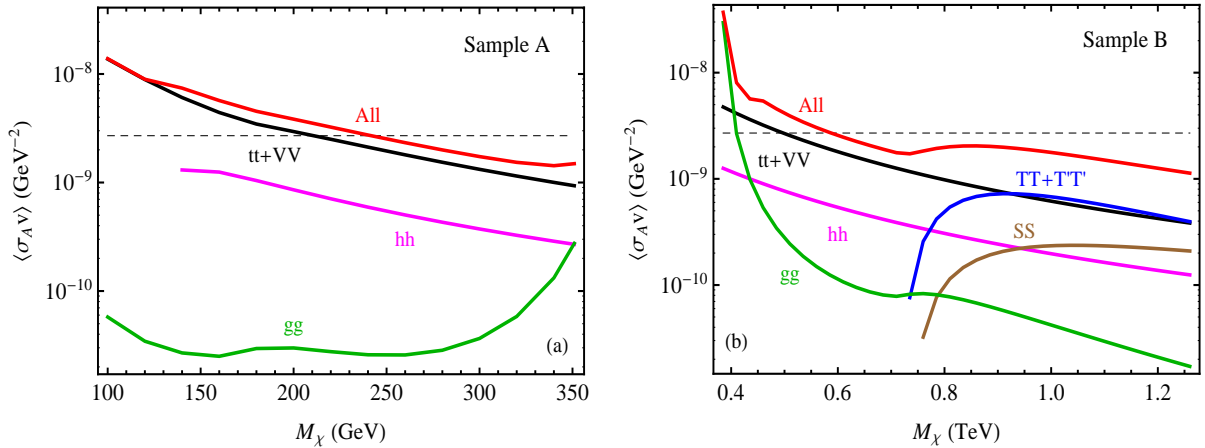


Figure 4: Thermal averaged cross section for DM annihilation, as a function of the DM mass M_χ for Sample-A [plot-(a)] and Sample-B [plot-(b)].

particles and SS . For our analysis, we summarize the nonzero coupling constants of relevant vertices around $\alpha \sim 0$ region,

$$\lambda_{\chi\chi S} = -\lambda_5 u, \quad \lambda_{\chi\chi h} = -\lambda_6 v, \quad \lambda_{\chi\chi hh} = -\lambda_6, \quad \lambda_{\chi\chi SS} = -\lambda_5, \quad \lambda_{hh h} = -6\lambda_1 v, \quad \lambda_{hh S} = -\lambda_3 u, \quad \lambda_{hSS} = -\lambda_3 v. \quad (5.1)$$

The only parameter unspecified in our samples (3.5) is μ_3 , which is connected to the DM mass M_χ . Since it is irrelevant to the stability analysis in Sec. 4, we treat it as a free parameter corresponding to the DM mass.

We compute the thermal averaged cross sections for DM annihilations. In Figs. 4(a)-(b), we present them as functions of the DM mass M_χ for Sample-A and Sample-B. The black dashed line shows the typical cross section $\langle\sigma_{AV}\rangle = 2.7 \times 10^{-9} \text{ GeV}^{-2}$, which corresponds to the observed DM relic density. The solid curves represent our theory prediction. For Sample-A, we consider the lighter mass region $M_\chi < 375 \text{ GeV}$, as shown in Fig. 4(a). With the sample input $\lambda_{\chi\chi S} = -57 \text{ GeV}$, the annihilation cross section is dominated by $t\bar{t}$ and VV final states. They come from the Higgs exchange and are sensitive to λ_6 . To produce the observed relic density, we find that the typical DM mass is around $M_\chi = 240 \text{ GeV}$. For Sample-B, we consider the larger mass range $M_\chi > 375 \text{ GeV}$, as shown in Fig. 4(b). With the sample input $\lambda_{\chi\chi S} = -360 \text{ GeV}$, $t\bar{t}$ and VV channels still give the main contribution. The annihilation cross sections of $\chi\chi \rightarrow \mathcal{T}\mathcal{T}, \mathcal{T}'\mathcal{T}'$ become barely comparable when $M_\chi > M_{\mathcal{T}(\mathcal{T}')}$. To generate the observed DM relic density, we find the DM mass around $M_\chi = 588 \text{ GeV}$, which is mainly determined by $t\bar{t}$ and VV cross sections.

5.2. Dark Matter Production at the LHC Run-2

An important case is that the DM mass falls into the region $M_\chi < M_S/2$, as described by Sample-A, so the 750 GeV new resonance has significant invisible decays $S \rightarrow \chi\chi$. The invisible decay width of S is

$$\Gamma(S \rightarrow \chi\chi) = \frac{\lambda_{\chi\chi S}^2}{32\pi M_S} \sqrt{1 - \frac{4M_\chi^2}{M_S^2}}. \quad (5.2)$$

In Fig. 5(a), we present the branching fractions of S decays as functions of the invisible width $\Gamma(S \rightarrow \chi\chi)$. To generate the right amount of DM relic abundance requires $M_\chi = 240 \text{ GeV}$, as shown in Fig. 4(a). This is marked by the black vertical dashed line in Fig. 5(a). At $M_\chi = 240 \text{ GeV}$, the corresponding invisible width and branching fraction are, $\Gamma(S \rightarrow \chi\chi) = 0.033 \text{ GeV}$ and $\text{Br}(S \rightarrow \chi\chi) = 51\%$. Under narrow width assumption, the diphoton cross section is related to $\text{Br}(S \rightarrow \chi\chi)$ as follows,

$$\sigma(pp \rightarrow S \rightarrow \gamma\gamma) = \sigma_0(pp \rightarrow S \rightarrow \gamma\gamma) [1 - \text{Br}(S \rightarrow \chi\chi)], \quad (5.3)$$

where $\sigma_0(pp \rightarrow S \rightarrow \gamma\gamma) = 7.3 \text{ fb}$ is the cross section at 13 TeV assuming zero invisible decay width, as given in Eq.(3.6) for Sample-A. The diphoton cross section is depicted by the black solid curve as a function of M_χ in Fig. 5(b). The vertical dashed line denotes $M_\chi = 240 \text{ GeV}$, at which we have

$$\sigma(pp \rightarrow S \rightarrow \gamma\gamma) \simeq 3.6 \text{ fb}, \quad (\text{Sample-A}). \quad (5.4)$$

In passing, Ref. [29] studied invisible decays of the 750 GeV resonance into a pair of Dirac fermion DM in a simplified DM model.

The LHC can probe the invisible decay $S \rightarrow \chi\chi$ of our model via mono-jet searches. When S is produced by gg fusion, an extra gluon can be radiated from either the initial gluons or the heavy quarks in the loop. This

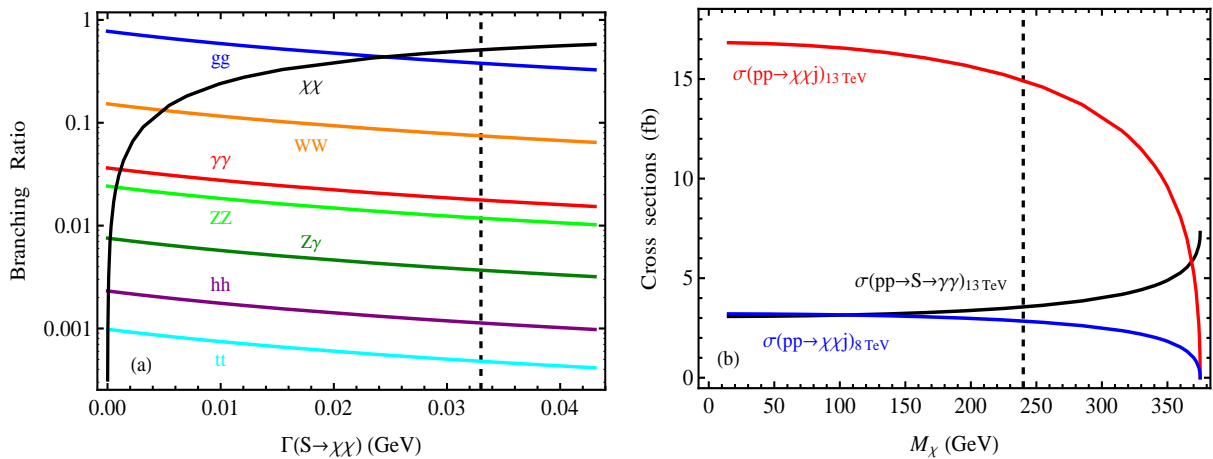


Figure 5: (a). Branching ratios of S decay as functions of invisible width $\Gamma(S \rightarrow \chi\chi)$. (b). DM production cross section with mono-jet as a function of mass M_χ . The red and blue curves present the parton level mono-jet cross sections at the LHC (13TeV) and the LHC (8TeV), respectively, under preselection cuts: $p_{Tj} > 120$ GeV, $|\eta_j| < 2$, and $E_T^{\text{miss}} > 150$ GeV. The black curve shows the diphoton cross section $\sigma(pp \rightarrow S \rightarrow \gamma\gamma)$ at the LHC (13TeV). The vertical dashed line denotes the demanded DM mass for realizing the observed thermal relic density.

channel has been studied by ATLAS at 8 TeV [30]. We generate $pp \rightarrow j\chi\chi$ events with $M_\chi = 240$ GeV by using MadGraph5_aMC@NLO [31][32], and apply the preselection cuts, $p_{Tj} > 120$ GeV, $|\eta_j| < 2$, and $E_T^{\text{miss}} > 150$ GeV. The cross section is 2.8 fb at the LHC (8TeV), which only produces 57 events with 20 fb^{-1} integrated luminosity. On the other hand, the uncertainty is still quite large. Even for the most sensitive signal region SR9 with $E_T^{\text{miss}} > 700$ GeV, our signal is about the same size as the uncertainty. Since only preselection cuts are applied in our simulation, the signals are small enough to evade the current bound. The parton level cross section under the preselection cuts for $\sqrt{s} = 13$ TeV and $\sqrt{s} = 8$ TeV are depicted by the red and blue curves in Fig. 5(b). We see that compared to the case of $\sqrt{s} = 8$ TeV, the mono-jet cross section at $\sqrt{s} = 13$ TeV is about 5 times larger, $\sigma(pp \rightarrow j\chi\chi) \simeq 15$ fb for $M_\chi = 240$ GeV. This signal may become observable with higher integrated luminosity at the Run-2. For Sample-B with $M_\chi > 375$ GeV, a $\chi\chi$ pair could only be produced via the off-shell exchange of S . This makes the mono-jet cross section even smaller.

5.3. Dark Matter Direct Detection

In the present model, DM interacts with the nucleon via exchanging both the Higgs boson h (125GeV) and the new particle S (750 GeV). In the $\alpha \sim 0$ region, h interacts with the quark and gluon content in the nucleon, while S only interacts with the gluons via heavy quark triangle-loops. The DM-nucleon interaction is spin-independent. We derive the DM recoil cross section,

$$\sigma_{\text{SI}} = \frac{m_N^2}{\pi(M_\chi + m_N)^2} (G_{h,N} + G_{S,N})^2, \quad G_{h,N} = \frac{\lambda_{\chi\chi h} f_N m_N}{2vM_h^2}, \quad G_{S,N} = \frac{2\lambda_{\chi\chi S} \bar{y}_S m_N}{27\sqrt{2}M_T M_S^2} \left(1 - \sum_{q=u,d,s} f_{N,q} \right), \quad (5.5)$$

where the nucleon mass $m_N = 0.939$ GeV is the averaged mass of proton and neutron. For the effective form factor, we use $f_N = 0.345$ [33], and $(f_{N,u}, f_{N,d}, f_{N,s}) = (0.014, 0.036, 0.118)$ [34]. In Fig. 6, we present the spin-independent cross section as a function of the DM mass M_χ for Sample-A and Sample-B by the red curves. Note that the contribution from S -exchange is heavily suppressed by $M_S = 750$ GeV. Given the cubic couplings $(\lambda_{\chi\chi h}, \lambda_{\chi\chi S})$ in Sample-A and Sample-B, we find that the DM-nucleon cross section is dominated by h -exchange. The black dot denotes our prediction by imposing the constraint of observed thermal relic density. Currently, the strongest constraint on the spin-independent cross section comes from LUX experiment [35] with the shaded region excluded at 90% C.L. Figs. 6(a)-(b) show that our prediction (black dot) is currently viable. But it is within the reach of the projected sensitivity of the upcoming Xenon1T [36], as represented by the blue dashed curve.

5.4. Dark Matter Indirect Detection

The DM annihilations can be also probed via indirect detections in the sky. The first type is the gamma-ray spectral lines that arise from the DM annihilation $\chi\chi \rightarrow \gamma X$, where X denotes any other possible SM bosons. In the present

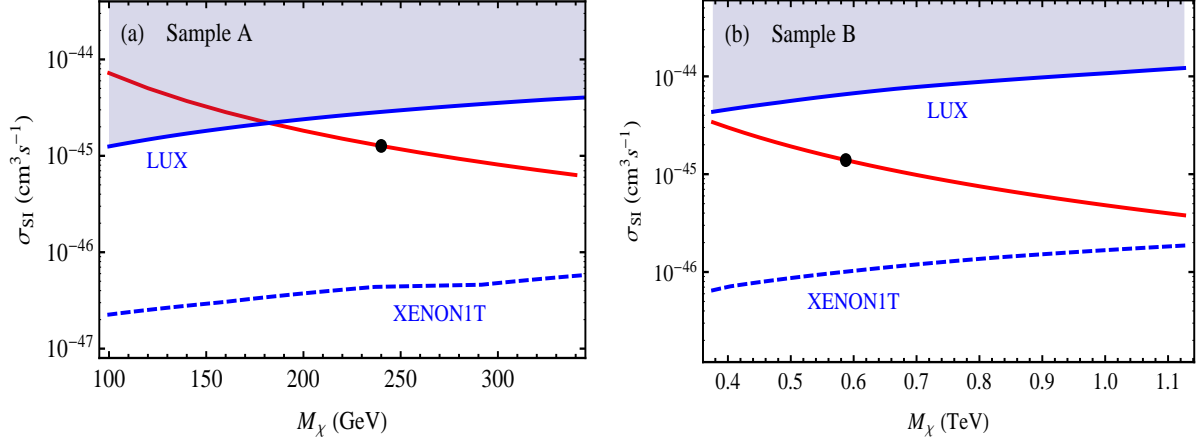


Figure 6: DM-nucleon spin-independent cross section as a function of M_χ for Sample-A [plot-(a)] and Sample-B [plot-(b)]. In each plot, the red curve presents our prediction, and the black dot is dictated by further imposing the constraint of the observed DM relic density. The shaded region is excluded by the LUX measurements, and the region above the blue dashed curve will be probed by the upcoming XENON1T experiment.

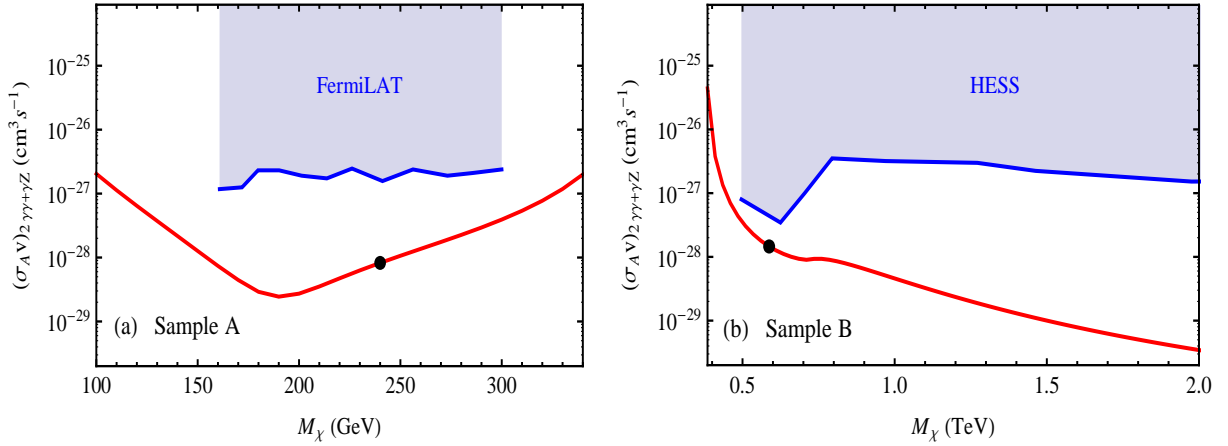


Figure 7: Prediction of $2(\sigma_A v)_{\gamma\gamma} + (\sigma_A v)_{\gamma Z}$ as a function of M_χ for Sample-A [plot-(a)] and Sample-B [plot-(b)]. In each plot, the red curve presents the theory prediction, and the black dot is dictated by further imposing the constraint of the observed DM relic density. The shaded regions in plots (a) and (b) are excluded by Fermi-LAT and HESS experiments, respectively.

model, we have annihilation processes $\chi\chi \rightarrow \gamma\gamma$ and $\chi\chi \rightarrow \gamma Z$. In the parameter region of $\alpha \sim 0$, we derive the annihilation cross sections,

$$(\sigma_A v)_{\gamma\gamma} = \frac{\alpha^2 M_\chi^2}{4\pi^3} \left| \frac{\lambda_{\chi\chi h}}{(4M_\chi^2 - M_h^2)v} \left[\sum_{f=\text{SM}} N_{cf} Q_f^2 F_{1/2}(\tau_{\chi f}) + F_1(\tau_{\chi W}) \right] + \frac{\lambda_{\chi\chi S}}{4M_\chi^2 - M_S^2} \frac{\tilde{y}_S}{\sqrt{2}M_{\mathcal{T}f=\mathcal{T},\mathcal{T}'}} \sum N_{cf} Q_f^2 F_{1/2}(\tau_{\chi f}) \right|^2, \quad (5.6a)$$

$$(\sigma_A v)_{\gamma Z} = \frac{8\alpha^2 M_\chi^2}{\pi^3} \left| \frac{\lambda_{\chi\chi h}}{(4M_\chi^2 - M_h^2)v} \left[\sum_{f=\text{SM}} N_{cf} Q_f (T_f^{3L} - 2Q_f s_W^2) B_{1/2}(\tau_{\chi f}, \eta_f) + B_1(\tau_{\chi W}, \eta_W) \right] + \frac{\lambda_{\chi\chi S}}{4M_\chi^2 - M_S^2} \frac{\tilde{y}_S}{\sqrt{2}M_{\mathcal{T}f=\mathcal{T},\mathcal{T}'}} \sum N_{cf} Q_f (T_f^{3L} - 2Q_f s_W^2) B_{1/2}(\tau_{\chi f}, \eta_f) \right|^2, \quad (5.6b)$$

where $\alpha = 1/128$, $\tau_{\chi f} = M_f^2/M_\chi^2$, $\eta_f = 4M_f^2/M_Z^2$, and $N_{cf} = 3$ (1) corresponds to the color factor of quarks (leptons). The loop factors $F_{1,1/2}(\tau)$ and $B_{1,1/2}(\tau, \eta)$ are defined in Appendix A. The upper bound on the annihilation $\chi\chi \rightarrow \gamma X$ can be extracted from galactic center γ -ray line search, i.e., Fermi-LAT in low photon energy range [37] and HESS in high energy range [38]. Provided that the DM annihilations into $\gamma\gamma$ and γZ are the only sources to generate gamma ray line, we may implement the constraint on the quantity $2(\sigma_A v)_{\gamma\gamma} + (\sigma_A v)_{\gamma Z}$. Fig. 7 presents this quantity as a function of M_χ for Sample-A [plot-(a)] and Sample-B [plot-(b)] by red curves. The upper bounds of Fermi-LAT and HESS are around $10^{-27} \text{ cm}^3 \text{ s}^{-1}$. In each plot, the red curve is our theory prediction and the black dot represents our prediction after imposing the constraint of the observed DM relic density. Plot-(a) shows that our

Sample-A prediction is fully safe from the bound of Fermi-LAT. For Sample-B, the bound from HESS in plot-(b) is also not yet strong enough, but is quite close to our prediction.

The second type of gamma ray signal is the diffuse continuum spectrum from secondary production of photons from primary DM annihilations, $\chi\chi \rightarrow W^+W^-, ZZ, b\bar{b}, \tau^+\tau^-, \mu^+\mu^-$. The secondary photon is then initiated from the final state radiation or hadronization with decays $\pi^0 \rightarrow \gamma\gamma$. The latest results come from the 4-years data of Fermi-LAT observation of 15 Milky Way dwarf spheroidal satellite galaxies [39]. In the near future, the next generation experiments with better angular resolution (such as CTA [40]) will largely improve the sensitivity over a wider mass range. We may extract the conservative constraint by taking into account of the branching ratio for each detection channel. In Sample-A and Sample-B, these final states arise from the light Higgs exchange. We find that the predicted cross sections are far below the current upper bounds from Fermi-LAT and HESS. But their predictions are within the reach of future experiments via W^+W^- and ZZ channels.

Another way of DM indirect detection is to measure the cosmic ray antiprotons, which could be produced from hadronization of the primary products of DM annihilations. Considering the uncertainty in modeling the antiproton propagation in galaxies, Ref. [41] derived limits on the annihilation cross sections with W^+W^- and $b\bar{b}$ final states from AMS02 p/\bar{p} ratio measurement [42]. The antiproton constraints are only slightly stronger than that from Fermi-LAT in the small mass region, $M_\chi \lesssim 200$ GeV. They impose no real constraints on our samples. In passing, the antiproton constraint on gg final state was discussed in [43], showing that the gg final state is dominant at high energy end of the spectrum and AMS02 may have potential to probe this signature.

6. Conclusions

The observed diphoton excess at the LHC Run-2 [1][2], if confirmed, would point to an exciting direction of new physics beyond the SM. In this work, we constructed a minimal model which is well motivated by realizing dark matter candidate, ensuring vacuum stability, and generating cosmic inflation. With this we provided an explanation of the recently observed 750 GeV new resonance at the LHC Run-2. In addition to the SM particle spectrum, our model contains one complex singlet scalar \mathcal{S} and one vector-like weak doublet quark $\mathbb{T} = (\mathcal{T}', \mathcal{T})^T$. The real component S of the singlet \mathcal{S} has Yukawa interaction with \mathbb{T} and can act as the 750 GeV resonance. Since $(\mathcal{T}', \mathcal{T})$ carry hypercharge $\frac{7}{6}$ and thus larger electric charges $(\frac{5}{3}, \frac{2}{3})$ than the SM quark doublet, this makes S have larger decay rate into diphotons. We demonstrated that S can serve as the 750 GeV new resonance and explain the observed excess of diphoton signals. Furthermore, the imaginary component χ of the singlet \mathcal{S} is a CP-odd pseudoscalar and the CP symmetry ensures χ to be a stable DM candidate. We find that this construction is rather economical and predictive, where the free parameters in the scalar potential are almost fully determined by accommodating the 750 GeV resonance, the vacuum stability of scalar potential, and the DM relic abundance. For explicit demonstration, we constructed two numerical Samples A and B to study the phenomenology. In section 3, we analyzed the prediction of $S(750\text{GeV})$, including its production and decays at the LHC Run-2. Further tests will be given by the upcoming LHC runs in this year. Then, in section 4 we studied the constraints of vacuum stability and the realization of Higgs inflation in our model. We derived the constraints from the DM relic abundance in section 5.1, and analyzed the mono-jet signals $pp \rightarrow jS \rightarrow j\chi\chi$ at the LHC Run-2 in section 5.2. Finally, we presented the constraints from the DM direct and indirect searches in sections 5.3–5.4.

Appendix A. Formulas for New Scalar Decays

In this Appendix, we derive the partial widths of the heavy scalar S decaying into the SM particles (gauge bosons, Higgs bosons and fermions). We present the following general formulas, which are used in our current analyses,

$$\Gamma(S \rightarrow hh) = \frac{G_{S hh}^2}{32\pi M_S} \sqrt{1 - \frac{4M_h^2}{M_S^2}}, \quad (\text{A.1a})$$

$$\Gamma(S \rightarrow f\bar{f}) = \xi_{S ff}^2 \frac{N_c g^2 m_f^2}{32\pi M_W^2} M_S \left(1 - 4\frac{m_f^2}{M_S^2}\right)^{3/2}, \quad (\text{A.1b})$$

$$\Gamma(S \rightarrow WW) = \xi_{S WW}^2 \frac{g^2 M_S}{64\pi} \frac{\sqrt{1-x_W}}{x_W} (4 - 4x_W + 3x_W^2), \quad (\text{A.1c})$$

$$\Gamma(S \rightarrow ZZ) = \xi_{S ZZ}^2 \frac{g^2 M_S}{128\pi} \frac{\sqrt{1-x_Z}}{x_W} (4 - 4x_Z + 3x_Z^2), \quad (\text{A.1d})$$

$$\Gamma(S \rightarrow \gamma\gamma) = \frac{\alpha^2 g^2}{256\pi^3} \frac{M_S}{x_W} \left| \sum_f N_{cj} Q_f^2 \xi_{S ff} F_{1/2}(\tau_f) + \xi_{S WW} F_1(\tau_W) \right|^2, \quad (\text{A.1e})$$

$$\Gamma(S \rightarrow gg) = \frac{\alpha_s^2 g^2}{128\pi^3} \frac{M_S}{x_W} \left| \sum_f \xi_{Sff} F_{1/2}(\tau_f) \right|^2, \quad (\text{A.1f})$$

$$\Gamma(S \rightarrow Z\gamma) = \frac{\alpha^2 g^2}{128\pi^3} \frac{M_S}{x_W} \left| \sum_f \xi_{Sff} N_{cf} Q_f (T_f^{3L} - 2Q_f s_W^2) B_{1/2}(\tau_f, \eta_f) + \xi_{SWW} B_1(\tau_W, \eta_W) \right|^2, \quad (\text{A.1g})$$

where $x_Z = 4M_Z^2/M_S^2$, $x_W = 4M_W^2/M_S^2$, $\tau_f = 4M_f^2/M_S^2$, $\eta_f = 4M_f^2/M_Z^2$, and the color factor $N_{cf} = 3$ (1) for quarks (leptons). For convenience, in the above we have rescaled the coupling ratios for $\mathcal{T}(\mathcal{T}')$ in Table 2 as, $\xi_{S\mathcal{T}\mathcal{T}(\mathcal{T}'\mathcal{T}')} = c_\alpha \tilde{y}_S v / (\sqrt{2} M_{\mathcal{T}(\mathcal{T}'')})$. The loop functions $F_1(\tau_f)$ and $F_{1/2}(\tau_f)$ are defined as,

$$F_1 = 2 + 3\tau [1 + (2 - \tau)f(\tau)], \quad F_{1/2} = -2\tau [1 + (1 - \tau)f(\tau)], \quad (\text{A.2a})$$

with

$$f(\tau) = \begin{cases} (\sin^{-1} \sqrt{1/\tau})^2, & \text{if } \tau \geq 1, \\ -\frac{1}{4} [\ln(\eta_+/\eta_-) - i\pi]^2, & \text{if } \tau < 1, \end{cases} \quad (\text{A.2b})$$

where $\eta_\pm = 1 \pm \sqrt{1 - \tau}$. The loop functions $B_1(\tau_f, \eta_f)$ and $B_{1/2}(\tau_f, \eta_f)$ are defined as,

$$B_1(\tau, \eta) = -t_W^{-1} [4(3 - t_W^2)I_2(\tau, \eta) + ((1 + 2\tau)t_W^2 - (5 + 2\tau))I_1(\tau, \eta)], \quad (\text{A.3a})$$

$$B_{1/2}(\tau, \eta) = \frac{-2}{s_W c_W} [I_1(\tau, \eta) - I_2(\tau, \eta)], \quad (\text{A.3b})$$

$$I_1(\tau, \eta) = \frac{\tau\eta}{2(\tau - \eta)} + \frac{\tau^2\eta^2}{2(\tau - \eta)^2} [f(\tau) - f(\eta)] + \frac{\tau^2\eta}{(\tau - \eta)^2} [g(\tau) - g(\eta)], \quad (\text{A.3c})$$

$$I_2(\tau, \eta) = -\frac{\tau\eta}{2(\tau - \eta)} [f(\tau) - f(\eta)], \quad (\text{A.3d})$$

$$g(\tau) = \begin{cases} \sqrt{\tau - 1} \arcsin \sqrt{1/\tau}, & \tau \geq 1, \\ \frac{1}{2} \sqrt{1 - \tau} [\log(\eta_+/\eta_-) - i\pi], & \tau < 1, \end{cases} \quad (\text{A.3e})$$

where we have used the abbreviations, $(s_W, c_W) = (\sin \theta_W, \cos \theta_W)$ and $t_W = \tan \theta_W$, with θ_W denoting the weak mixing angle. For $h \rightarrow gg$ in the SM, the QCD corrections will introduce an enhancement factor of $K(M_h) \approx 1.5$ for $M_h = 750 \text{ GeV}$ [44][45]. For the current case of $S(750 \text{ GeV})$, the decay width of $S \rightarrow gg$ is generated by $\mathcal{T}(\mathcal{T}')$ triangle-loops instead of the top loop. But, the QCD K -factor is expected to be similar to the SM case. So we use the SM K -factor as a reasonable estimate, $K(M_S) \approx 1.5$.

There is one complication for the S decays into weak gauge boson pairs WW and ZZ . At tree level, S could couple with WW and ZZ through mixing with the SM Higgs boson h . The corresponding decay widths are given in (A.1c) and (A.1d), respectively. But, they should vanish when the mixing angle $\alpha \rightarrow 0$, or, becomes negligible for $\alpha \lesssim 10^{-3}$. In this case, the $\mathcal{T}(\mathcal{T}')$ triangle-loop corrections become dominant. Here we derive the decay width up to one-loop level,

$$\Gamma(S \rightarrow WW) = \frac{|\mathcal{M}(S \rightarrow WW)|^2}{16\pi M_S}, \quad \Gamma(S \rightarrow ZZ) = \frac{|\mathcal{M}(S \rightarrow ZZ)|^2}{32\pi M_S}, \quad (\text{A.4})$$

with the decay matrix elements parametrized as,

$$\mathcal{M}(S \rightarrow V_j V_{j'}) = \{i c_0 g^{\mu\nu} - c_1 [(k_1 \cdot k_2) g^{\mu\nu} - k_1^\nu k_2^\mu]\} \epsilon_{\mu j}(k_1) \epsilon_{\nu j'}(k_2), \quad (\text{A.5a})$$

where $V = W, Z$, and $j, j' = (+, -, 0)$ denote the three polarizations of weak gauge boson V^μ . In the above decay amplitude, the coefficients (c_0, c_1) are given by the tree-level and triangle-loop contributions, respectively. For the loop contribution c_1 , we compute the triangle-loop by setting the final state VV be massless, which is well justified due to $M_S^2 \gg M_V^2$. We summarize the results as follows,

$$S \rightarrow WW: \quad c_0 = \sin \alpha \frac{2M_W^2}{v}, \quad c_1 = \frac{\alpha N_c}{2s_w^2 \pi v} A(\tau), \quad (\text{A.5b})$$

$$S \rightarrow ZZ: \quad c_0 = \sin \alpha \frac{2M_Z^2}{v}, \quad c_1 = \frac{\alpha N_c}{c_w^2 s_w^2 \pi v} \left(\frac{1}{2} - s_w^2 + \frac{29}{9} s_w^4 \right) A(\tau). \quad (\text{A.5c})$$

Since the two vector-like quarks \mathcal{T} and \mathcal{T}' have nearly degenerate masses, we have $\tau = 4M_{\mathcal{T}'}^2/M_S^2 \simeq 4M_{\mathcal{T}}^2/M_S^2$, and $A(\tau) = -\frac{1}{2}F_{1/2}(\tau)$. We also note that for the c_1 related loop contributions, the longitudinal polarization has negligible contributions to the decay amplitude (A.5a). Since $M_S \gg M_V$, we can apply the equivalence theorem [15] to replace the final state longitudinal component V_L^a by the corresponding would-be Goldstone boson π^a . But we find that the Goldstone amplitude is nearly vanishing because the Yukawa couplings of π^a with $\mathcal{T}(\mathcal{T}')$ are highly suppressed by the tiny mixing angles θ_{Rj} according to Eqs. (2.3)-(2.4) and θ_{Rj} formula below them. Thus, for the triangle-loop contributions it is a good approximation to treat the final state VV to be massless and ignore the longitudinal polarization. As a consistent check, we find that including longitudinal polarization to the final state VV at one-loop could only affect the partial decay width by about (1–2)% and has negligible effect.

Fig. 1 clearly shows that the effect of triangle-loop contributions dominate $\text{Br}(S \rightarrow WW, ZZ)$ and the WW/ZZ branching fraction curves become nearly flat over the small α region of $\alpha \lesssim 2 \times 10^{-3}$, where the tree-level contributions are negligible due to the severe $\sin\alpha$ suppression.

Appendix B. One-Loop β Functions from New Couplings

In this Appendix, we present the additional terms in the one-loop β functions which are induced by the new couplings of our model. We first consider the couplings $(\lambda_1, y_{ij}, g_s, g, g')$, which also appear in the SM. We analyze their β functions and find the following new terms,

$$\Delta\beta_{\lambda_1} = \frac{1}{(4\pi)^2} \left(\frac{1}{2}\lambda_3^2 + \frac{1}{2}\lambda_6^2 \right), \quad \Delta\beta_{y_i} = 0, \quad \Delta\beta_{g_s} = \frac{2}{3(4\pi)^2} g_s^2, \quad \Delta\beta_g = \frac{2}{3(4\pi)^2} g^2, \quad \Delta\beta_{g'} = \frac{49}{9(4\pi)^2} g'^2. \quad (\text{B.1})$$

Then, we derive the one-loop β functions for the new couplings of our model,

$$\beta_{\lambda_2} = \frac{1}{(4\pi)^2} \left(18\lambda_2^2 + 2\lambda_3^2 + \frac{1}{2}\lambda_5^2 + 24\lambda_2\tilde{y}_S^2 - 12\tilde{y}_S^4 \right), \quad (\text{B.2a})$$

$$\beta_{\lambda_3} = \frac{1}{(4\pi)^2} \left[\lambda_3 \left(12\lambda_1 + 6\lambda_2 + 4\lambda_3 + 6y_t^2 + 12\tilde{y}_S^2 - \frac{9}{2}g^2 - \frac{3}{2}g'^2 \right) + \lambda_5\lambda_6 \right], \quad (\text{B.2b})$$

$$\beta_{\lambda_4} = \frac{1}{(4\pi)^2} \left(18\lambda_4^2 + \frac{1}{2}\lambda_5^2 + 2\lambda_6^2 \right), \quad (\text{B.2c})$$

$$\beta_{\lambda_5} = \frac{1}{(4\pi)^2} \left(6\lambda_2\lambda_5 + 6\lambda_4\lambda_5 + 4\lambda_3\lambda_6 + 12\lambda_5\tilde{y}_S^2 \right), \quad (\text{B.2d})$$

$$\beta_{\lambda_6} = \frac{1}{(4\pi)^2} \left[\lambda_6 \left(12\lambda_1 + 6\lambda_4 + 4\lambda_6 + 6y_t^2 + 6\tilde{y}_S^2 - \frac{9}{2}g^2 - \frac{3}{2}g'^2 \right) + \lambda_3\lambda_5 \right], \quad (\text{B.2e})$$

$$\beta_{\tilde{y}_S} = \frac{\tilde{y}_S}{(4\pi)^2} \left(\frac{9}{2}\tilde{y}_S^2 - 8g_s^2 - \frac{9}{4}g^2 - \frac{49}{6}g'^2 \right). \quad (\text{B.2f})$$

For the Yukawa couplings in the above formulas, we only need to keep the top quark Yukawa coupling y_t and the heavy quark \mathbb{T} Yukawa coupling \tilde{y}_S , as explained in the text.

Acknowledgments:

We thank Mingshui Chen, Xin Chen, and Weiming Yao for discussing the ATLAS and CMS data concerning the diphoton excess. This work was supported in part by National NSF of China (under grants Nos. 11275101 and 11135003) and National Basic Research Program (under grant No. 2010CB833000).

References

- [1] The ATLAS collaboration, ATLAS-CONF-2015-081, December 15, 2015.
- [2] The CMS Collaboration, CMS-PAS-EXO-15-004, December 15, 2015.
- [3] D. Buttazzo, A. Greljo, and D. Marzocca, Eur. Phys. J. C 76 (2016) 116 [arXiv:1512.04929 [hep-ph]].
- [4] G. Aad *et al.* [ATLAS Collaboration], Phys. Lett. B 716 (2012) 1 [arXiv:1207.7214 [hep-ex]]; S. Chatrchyan *et al.* [CMS Collaboration], Phys. Lett. B 716 (2012) 30 [arXiv:1207.7235 [hep-ex]].
- [5] L. D. Landau, Dokl. Akad. Nauk Ser. Fiz. 60 (1948) 207; C. N. Yang, Phys. Rev. 77 (1950) 242.
- [6] E.g., for a partial list, K. Harigaya and Y. Nomura, arXiv:1512.04850 [hep-ph]; Y. Mambriani, G. Arcadi, and A. Djouadi, arXiv:1512.04913 [hep-ph]; A. Angelescu, A. Djouadi, and G. Moreau, arXiv:1512.04921 [hep-ph]; M. Backovic, A. Mariotti, D. Redigolo, arXiv:1512.04917 [hep-ph]; S. Knapen, T. Melia, M. Papucci and K. Zurek, arXiv:1512.04928 [hep-ph]; D. Buttazzo, A. Greljo, and D. Marzocca, arXiv:1512.04929 [hep-ph]; R. Franceschini *et al.*, arXiv:1512.04933 [hep-ph]; Stefano Di Chiara, L. Marzola and M. Raidal, arXiv:1512.04939 [hep-ph]; A. Pilaftsis, arXiv:1512.04931 [hep-ph]; John Ellis, Sebastian A. R. Ellis, Jeremie Quevillon, Veronica Sanz, and Tevong You, arXiv:1512.05327 [hep-ph]; R. S. Gupta, S. Jager, Y. Kats, G. Perez and E. Stamou, arXiv:1512.05332 [hep-ph]; Shinya Matsuzaki and Koichi Yamawaki, arXiv:1512.05564 [hep-ph]; Q. H. Cao, Y. Liu, K. P. Xie, B. Yan and D. M. Zhang, arXiv:1512.05542 [hep-ph]; J. M. No, V. Sanz, J. Setford, arXiv:1512.05700 [hep-ph]; D. Curtin and C. B. Verhaaren, arXiv:1512.05753 [hep-ph]; P. Agrawal,

- J. J. Fan, B. Heidenreich, M. Reece and M. Strassler, arXiv:1512.05775 [hep-ph]; O. Antipin, M. Mojaza, F. Sannino, arXiv:1512.06708 [hep-ph]; B. Dutta, Y. Gao, T. Ghosh, I. Gogoladze, and Tianjun Li, arXiv:1512.05439 [hep-ph]; A. Kobakhidze, F. Wang, L. Wu, J. M. Yang and M. Zhang, arXiv:1512.05585 [hep-ph]; W. Chao, R. Huo and J. H. Yu, arXiv:1512.05738 [hep-ph]; A. Falkowski, O. Slone and T. Volansky, arXiv:1512.05777 [hep-ph]; Y. Bai, J. Berger and R. Lu, arXiv:1512.05779 [hep-ph]; E. Gabrielli, K. Kannike, B. Mele, M. Raidal, C. Spethmann and H. Veermae, arXiv:1512.05961 [hep-ph]; R. Benbrik, C. H. Chen and T. Nomura, arXiv:1512.06028 [hep-ph]; H. Han, S. Wang and S. Zheng, arXiv:1512.06562 [hep-ph]; O. Antipin, M. Mojaza, and F. Sannino, arXiv:1512.06708 [hep-ph]; L. Berthier, J. M. Cline, W. Shepherd, and M. Trott, arXiv:1512.06799 [hep-ph]; X. J. Bi, Q. F. Xiang, P. F. Yin, and Z. H. Yu, arXiv:1512.06787 [hep-ph]; A. E. C. Hernandez and I. Nisandzic, arXiv:1512.07165 [hep-ph]; F. P. Huang, C. S. Li, Z. L. Liu and Y. Wang, arXiv:1512.06732 [hep-ph]; W. C. Huang, Y. L. Sming Tsai, Tzu-Chiang Yuan, arXiv:1512.07268 [hep-ph]; K. M. Patel and P. Sharma, arXiv:1512.07468 [hep-ph]; Q. H. Cao, S. L. Chen, and P. H. Gu, arXiv:1512.07541 [hep-ph]; W. Altmannshofer, J. Galloway, S. Gori, A. L. Kagan, A. Martin and J. Zupan, arXiv:1512.07616 [hep-ph]; M. x. Luo, K. Wang, T. Xu, L. Zhang, G. Zhu, arXiv:1512.06670 [hep-ph]; Mikael Chala, Michael Duerr, Felix Kahlhoefer, Kai Schmidt-Hoberg, arXiv:1512.06833 [hep-ph]; J. Gu and Z. Liu, arXiv:1512.07624 [hep-ph]. M. Dhuria and G. Goswami, arXiv:1512.06782 [hep-ph]; L. J. Hall, K. Harigaya and Y. Nomura, arXiv:1512.07904 [hep-ph]; P. S. Bhupal Dev and Daniele Teresi, arXiv:1512.07243 [hep-ph]; B. C. Allanach, P. S. Bhupal Dev, S. A. Renner, and K. Sakurai, arXiv:1512.07645 [hep-ph]; P. S. Bhupal Dev, R. N. Mohapatra and Y. Zhang, arXiv:1512.08507 [hep-ph]; J. A. Casas, J. R. Espinosa and J. M. Moreno, arXiv:1512.07895 [hep-ph]; K. Cheung, P. Ko, J. S. Lee, J. Park, P. Y. Tseng, arXiv:1512.07853 [hep-ph]; J. Zhang and S. Zhou, arXiv:1512.07889 [hep-ph]; A. Salvio and A. Mazumdar, arXiv:1512.08184 [hep-ph]; Y. L. Tang and S. h. Zhu, arXiv:1512.08323 [hep-ph]; Haipeng An, Clifford Cheung, Yue Zhang, arXiv:1512.08378 [hep-ph]; J. Cao, F. Wang and Y. Zhang, arXiv:1512.08392 [hep-ph]; G. Li, Y. n. Mao, Y. L. Tang, C. Zhang, Y. Zhou and S. h. Zhu arXiv:1512.08255 [hep-ph]; Shinya Kanemura, Naoki Machida, Shinya Odori, Tetsuo Shindou, arXiv:1512.09053 [hep-ph]; S. Kanemura, K. Nishiwaki, H. Okada, Y. Orikasa, S. C. Park, R. Watanabe, 1512.09048 [hep-ph]; Y. Hamada, T. Noumi, S. Sun, and G. Shiu, arXiv:1512.08984 [hep-ph]; Y. Jiang, Y. Y. Li, and T. Liu, arXiv:1512.09127 [hep-ph]; L. Marzola, A. Racioppi, M. Raidal, F. R. Urban, H. Veermae, arXiv:1512.09136 [hep-ph]; H. Zhang, arXiv:1601.01355 [hep-ph]. S. Alexander and L. Smolin, arXiv:1601.03091 [hep-ph]; Abdelhak Djouadi, John Ellis, Rohini Godbole, Jeremie Quevillon, arXiv:1601.03696 [hep-ph]; X. F. Han, L. Wang, L. Wu, J. M. Yang, and M. Zhang, arXiv:1601.00534 [hep-ph]; P. Ko and T. Nomura, arXiv:1601.02490 [hep-ph]; L. V. Laperashvili, H. B. Nielsen, C. R. Das, arXiv:1601.03231 [hep-ph]; W. Chao, arXiv:1601.04678 [hep-ph]; arXiv:1512.06297 [hep-ph]; arXiv:1512.08484 [hep-ph]; J. Kawamura and Yuji Omura, arXiv:1601.07396 [hep-ph]; P. Ko, Yuji Omura, and C. Yu, arXiv:1601.00586 [hep-ph]; M. R. Buckley, arXiv:1601.04751 [hep-ph]; A. Salvio, F. Staub, A. Strumia, A. Urbano, arXiv:1602.01460 [hep-ph]; R. Ding, Y. Fan, L. Huang, C. Li, Tianjun Li, S. Raza, B. Zhu, arXiv:1602.00977 [hep-ph]; Y. J. Zhang, B. B. Zhou, and J. J. Sun, arXiv:1602.05539; E. Morgante, D. Racco, M. Rameez, and A. Riotto, arXiv:1603.05592 [hep-ph]; Stefano Di Chiara, A. Hektor, K. Kannike, L. Marzola, M. Raidal, arXiv:1603.07263 [hep-ph]; T. du Pree, K. Hahn, P. Harris, and C. Roskas, arXiv:1603.08525 [hep-ph]; M. T. Frandsen and I. M. Shoemaker, arXiv:1603.09354 [hep-ph].
- [7] E.g., J. R. Espinosa, G. F. Giudice, and A. Riotto, JCAP 0805 (2008) 002 [arXiv:0710.2484]; A. Kobakhidze and A. Spencer-Smith, Phys. Lett. B 722 (2013) 130 [arXiv:1301.2846]; K. Enqvist, T. Meriniemi, and S. Nurmi, JCAP 1310 (2013) 057 [arXiv:1306.4511]; V. Branchina and E. Messina, Phys. Rev. Lett. 111 (2013) 241801 [arXiv:1307.5193]; A. Salvio, Phys. Lett. B 727 (2013) 234 [arXiv:1308.2244]; M. Fairbairn and R. Hogan, Phys. Rev. Lett. 112 (2014) 201801 [arXiv:1403.6786]; K. Enqvist, T. Meriniemi and S. Nurmi, JCAP 1407 (2014) 025 [arXiv:1404.3699]; M. Herranen, T. Markkanen, S. Nurmi and A. Rajantie, Phys. Rev. Lett. 113 (2014) 211102 [arXiv:1407.3141]; V. Branchina, E. Messina and M. Sher, Phys. Rev. D 91 (2015) 013003 [arXiv:1408.5302]; K. Kamada, Phys. Lett. B 742 (2015) 126 [arXiv:1409.5078]; A. Shkerin and S. Sibiryakov, arXiv:1503.02586; A. Hook, J. Kearney, B. Shakya, and K. M. Zurek, JHEP 1501 (2015) 061 [arXiv:1404.5953]; John Kearney, H. Yoo, K. M. Zurek, Phys. Rev. D 91 (2015) 123537 [arXiv:1503.05193]; and references therein.
- [8] J. R. Espinosa, G. F. Giudice, E. Morgante, A. Riotto, L. Senatore, A. Strumia, N. Tetradis, JHEP 1509 (2015) 174 [arXiv:1505.04825].
- [9] F. L. Bezrukov and M. Shaposhnikov, Phys. Lett. B 659 (2008) 703 [arXiv:0710.3755]; F. Bezrukov, Class. Quant. Grav. 30 (2013) 214001 [arXiv:1307.0708].
- [10] A. O. Barvinsky, A. Y. Kamenshchik, A. A. Starobinsky, JCAP 0811 (2008) 021 [arXiv:0809.2104]; A. De Simone, M. P. Hertzberg, F. Wilczek, Phys. Lett. B 678 (2009) 1 [arXiv:0812.4946]; F. L. Bezrukov, A. Magnin, M. Shaposhnikov, Phys. Lett. B 675 (2009) 88 [arXiv:0812.4950]; C. P. Burgess, H. M. Lee, M. Trott, JHEP 0909 (2009) 103 [arXiv:0902.4465]; A. O. Barvinsky, A. Y. Kamenshchik, C. Kiefer, A. A. Starobinsky, C. F. Steinwachs, Eur. Phys. J. C 72 (2012) 2219 [arXiv:0910.1041]; F. Bezrukov, A. Magnin, M. Shaposhnikov, and S. Sibiryakov, JHEP 1101 (2011) 016 [arXiv:1008.5157]; C. P. Burgess, H. M. Lee, M. Trott, JHEP 0909 (2009) 103 [arXiv:0902.4465]; J. Ren, Z.-Z. Xianyu, H.-J. He, JCAP 1406 (2014) 032 [arXiv:1404.4627]; and references therein.
- [11] E.g., Y. Hamada, H. Kawai, and K. Oda, JHEP 1407 (2014) 026 [arXiv:1404.6141]; N. Haba and R. Takahashi, Phys. Rev. D 89 (2014) 115009 [arXiv:1404.4737]; J. Rubio and M. Shaposhnikov, Phys. Rev. D 90 (2014) 027307 [arXiv:1406.5182]; Z.-Z. Xianyu and H.-J. He, JCAP 1410 (2014) 083 [arXiv:1407.6993 [astro-ph.CO]]; J. Ellis, H.-J. He, Z.-Z. Xianyu, Phys. Rev. D 91 (2015) 021302 (R) [arXiv:1411.5537]; S. Ferrara, R. Kallosh, A. Linde, A. Marrani, and A. Van Proeyen, Phys. Rev. D 82 (2010) 045003 [arXiv:1004.0712]; Phys. Rev. D 83 (2011) 025008 [arXiv:1008.2942]; M. Arai, S. Kawai, and N. Okada, Phys. Rev. D 84 (2011) 123515 [arXiv:1107.4767]; A. Salvio, Phys. Lett. B 743 (2015) 428 [arXiv:1501.03781]; N. Okada and Q. Shafi, Phys. Lett. B 747 (2015) 223 [arXiv:1501.05375 [hep-ph]]; A. Salvio and A. Mazumdar, Phys. Lett. B 750 (2015) 194 [arXiv:1506.07520]; and references therein.
- [12] H.-J. He and Z.-Z. Xianyu, JCAP 1410 (2014) 019 [arXiv:1405.7331].
- [13] H.-J. He, T. M. P. Tait, C.-P. Yuan, Phys. Rev. D 62 (2000) 011702 (R) [hep-ph/9911266].
- [14] E.g., S. Knapen, T. Melia, M. Papucci, and K. Zurek, arXiv:1512.04928 [hep-ph].
- [15] For a comprehensive review, H.-J. He, Y.-P. Kuang, C.-P. Yuan, DESY-97-056 and arXiv:hep-ph/9704276.
- [16] M. Buchkremer and A. Schmidt, Adv. High Energy Phys. 2013, 690254 (2013) [arXiv:1210.6369 [hep-ph]].
- [17] G. Aad *et al.* [ATLAS Collaboration], Phys. Rev. D 92, 112007 (2015) [arXiv:1509.04261 [hep-ex]].
- [18] A. D. Martin, W. J. Stirling, R. S. Thorne and G. Watt, Eur. Phys. J. C 63, 189 (2009) [arXiv:0901.0002 [hep-ph]].
- [19] CMS Collaboration, CMS-PAS-EXO-14-005.
- [20] G. Aad *et al.* [ATLAS Collaboration], Phys. Lett. B 738 (2014) 428 [arXiv:1407.8150 [hep-ex]].
- [21] V. Khachatryan *et al.* [CMS Collaboration], JHEP 1510 (2015) 144 [arXiv:1504.00936 [hep-ex]]; G. Aad *et al.* [ATLAS Collaboration], Eur. Phys. J. C 76 (2016) 45 [arXiv:1507.05930 [hep-ex]].
- [22] E.g., M. Low, A. Tesi and L. T. Wang, arXiv:1512.05328 [hep-ph].
- [23] R. N. Lerner and J. McDonald, Phys. Rev. D 83 (2011) 123522 [arXiv:1104.2468].
- [24] K. Allison, JHEP 1402 (2014) 040 [arXiv:1306.6931].
- [25] G. Degrassi *et al.*, JHEP 1208 (2012) 098 [arXiv:1205.6497].
- [26] J. Garcia-Bellido, D. G. Figueroa, and J. Rubio, Phys. Rev. D 79 (2009) 063531 [arXiv:0812.4624]; F. Bezrukov, D. Gorbunov, and M. Shaposhnikov, JCAP 0906 (2009) 029 [arXiv:0812.3622].
- [27] P. A. R. Ade *et al.* (Planck Collaboration), arXiv:1502.01589.
- [28] P. A. R. Ade *et al.* (Planck Collaboration), arXiv:1502.02114.
- [29] M. Backovic, A. Mariotti and D. Redigolo, JHEP 1603 (2016) 157 [arXiv:1512.04917 [hep-ph]].

- [30] G. Aad *et al.* [ATLAS Collaboration], Eur. Phys. J. C 75 (2015) 299 and C 75 (2015) 408 [arXiv:1502.01518 [hep-ex]].
- [31] J. Alwall *et al.*, JHEP 1407, 079 (2014) [arXiv:1405.0301 [hep-ph]].
- [32] V. Hirschi and O. Mattelaer, JHEP 1510, 146 (2015) [arXiv:1507.00020 [hep-ph]].
- [33] J. M. Cline, K. Kainulainen, P. Scott, C. Weniger, Phys. Rev. D 88 (2013) 055025 [D 92 (2015) 039906 (E)] [arXiv:1306.4710 [hep-ph]].
- [34] J. R. Ellis, A. Ferstl, K. A. Olive, Phys. Lett. B 481 (2000) 304 [arXiv:hep-ph/0001005].
- [35] D. S. Akerib *et al.*, [LUX Collaboration], arXiv:1310.8214 [astro-ph.CO].
- [36] E. Aprile *et al.* [XENON1T Collaboration], JCAP (2016) [arXiv:1512.07501 [physics.ins-det]].
- [37] M. Ackermann *et al.* [Fermi-LAT Collaboration], Phys. Rev. D 88 (2013) 082002 [arXiv:1305.5597 [astro-ph.HE]].
- [38] A. Abramowski *et al.* [H.E.S.S. Collaboration], Phys. Rev. Lett. 110 (2013) 041301 [arXiv:1301.1173 [astro-ph.HE]].
- [39] M. Ackermann *et al.* [Fermi-LAT Collaboration], Phys. Rev. D 89 (2014) 042001 [arXiv:1310.0828 [astro-ph.HE]].
- [40] B. S. Acharya, M. Actis, T. Aghajani, G. Agnetta, J. Aguilar, F. Aharonian, M. Ajello, A. Akhperjanian *et al.*, Astropart. Phys. 43 (2013) 3.
- [41] S. J. Lin, X. J. Bi, P. F. Yin, and Z. H. Yu, arXiv:1504.07230 [hep-ph].
- [42] AMS-02 Collaboration, Talks at the AMS Days at CERN, April 15-17, 2015.
- [43] A. Hektor and L. Marzola, arXiv:1602.00004 [hep-ph].
- [44] M. Spira, A. Djouadi, D. Graudenz and P. M. Zerwas, Nucl. Phys. B 453, 17 (1995) [arXiv:hep-ph/9504378].
- [45] A. Djouadi, Phys. Rept. 457 (2008) 1 [arXiv:hep-ph/0503172].